SOLAR CELLS

Homogenized chlorine distribution for >27% power conversion efficiency in perovskite solar cells

Zhuang Xiong[1,2]†, Qian Zhang[1,2]†, Kai Cai[1,2], Haitao Zhou[1,2], Qi Song[1,2], Zhaoyang Han[1,2], Shuaiqing Kang[3], Yaowen Li[3], Qi Jiang[1,2], Xingwang Zhang[1,2], Jingbi You[1,2]*

The spatial heterogeneity of halogen distribution in perovskite thin films represents a critical factor currently limiting both the power conversion efficiency and stability of solar cells. We identified pronounced through-film inhomogeneity in chlorine distribution in formamidinium lead iodide films, with the generally used additive methylammonium chloride. We demonstrated that incorporating alkali metal oxalates could effectively homogenize the chlorine distribution. These compounds underwent thermal dissociation, releasing alkali metal cations that selectively bound chloride ions, which considerably suppressed surface defects and eliminated interfacial barriers. A certified steady-state power conversion efficiency (PCE) of 27.2% (device area and measured mask area: 0.108 square cm and 0.074 square cm, respectively) in perovskite solar cells was achieved, and devices retained 86.3% of their initial PCE after 1529 hours of continuous maximum power point tracking (MPPT) under 1 Sun condition. Moreover, the unpassivated device maintained 82.8% of its original PCE under MPPT at 85°C aging under 1 Sun illumination after 1000 hours.

Perovskite solar cells have achieved certified power conversion efficiencies (PCEs) >26%, advancements primarily attributed to progress in film crystallization control, charge transport layer optimization, and interfacial passivation (*1*–*3*). A key factor in attaining high performance, in both one- and two-step deposition processing, is the incorporation of methylammonium chloride (MACl) additive (*4*–*8*), which reduced the nucleation barrier for intermediate state formation and decelerated crystal growth (*9*). Notably, the migration of MACl and its ultimate escape from the perovskite layer are processes highly sensitive to ambient moisture (*10*, *11*). However, precisely controlling the environmental humidity remains challenging, and the presence of moisture could induce surface aggregation of Cl, which hinders charge transport (*12*).

We identified that the perovskite films exhibited surface enrichment of chloride when using MACl as the additive, resulting in vertical compositional heterogeneity. This inhomogeneity promoted trap-assisted recombination and misalignment of energy levels, thereby suppressing interfacial carrier extraction. To address this issue, we introduced a homogenized vertical chlorine distribution (HVCD) strategy by adding alkali metal oxalates, such as potassium binoxalate (PB), into the perovskite precursors. During thermal annealing, PB dissociated and released K^+, which effectively bound chloride anions, leading to a HVCD in the films. This approach suppressed interfacial defects and minimized interfacial energy barriers. We have achieved high-performing inverted perovskite solar cells with a certified steady-state PCE of 27.2% (device area/measured mask area: 0.108 cm^2/0.074 cm^2, respectively). The HVCD devices also showed improved stability and maintained 98.8 and 85% of their initial performance after storage under dark for >3000 hours and continuous 85°C aging for 750 hours, respectively. Also, the HVCD devices maintained 86.3% of their original PCE after 1529 hours maximum power point tracking (MPPT) under 1 Sun condition. The unpassivated HVCD device retained 82.8% of its original PCE under MPPT and 85°C aging upon 1 Sun illumination after 1000 hours.

Homogenized vertical chlorine distribution

We prepared the perovskite precursor solution based on formamidinium lead iodide ($FAPbI_3$) with the addition of 19.5 mol % MACl and 6.5 mol % PbI_2, corresponding to a PbI_2:MACl molar ratio of 1:3, which was critical for obtaining high-quality perovskite films (*13*). After spin coating and vacuum flashing, the precursor films were annealed in a nitrogen atmosphere (movie S1). For the HVCD perovskite films, we added 0.7 mol % PB of $FAPbI_3$ as an additive for crystallization modulating (see supplementary materials for details).

To investigate the optoelectronic homogeneity of the resulting films, steady-state photoluminescence (SSPL) measurements were conducted from both the top and buried surfaces. The control perovskite film exhibited distinct emission peaks at 811 nm and 818 nm on top and buried surfaces, respectively, indicative of vertical phase segregation (Fig. 1A). By contrast, both surfaces showed identical emission peaks at 819 nm in the HVCD perovskite film, indicating uniform composition and vertical homogeneity (Fig. 1B).

X-ray photoelectron spectroscopy (XPS) revealed the chemical changes of the top surfaces. After annealing of the control precursor film, the surface concentration of Cl increased by more than one order of magnitude (Fig. 1C). This increase was attributed to the solvent's volatilization-induced migration of Cl^- anions from the bulk to the surface during annealing. This redistribution of anions resulted in substantial surface aggregation of Cl and consequently induced inhomogeneous crystallization and vertical phase segregation within the film (*14*–*16*). For the HVCD perovskite films, the surface concentration of Cl^- anions remained nearly the same after annealing, suggesting that the Cl^- anions were immobilized within the bulk (Fig. 1D).

Grazing-incident x-ray diffraction (GIXRD) was performed to investigate the crystal variation from the top surface (*17*). In the control perovskite film, a shift of (200) plane toward smaller diffraction peaks was observed by varying the grazing incident angle from 0.4° to 4° (Fig. 1E), whereas negligible changes occurred in the HVCD films (Fig. 1F). Similar results were obtained for the (100) planes (fig. S1). Conventional x-ray diffraction (XRD) of the control perovskite film (fig. S2) revealed a broadening diffraction peak corresponding to the (100) plane of cubic $FAPbI_3$, along with a shoulder peak at 28.15° associated with the (004) plane. These observations indicated the emergence of a tetragonal phase, which we attributed to the aggregation of MACl (*18*). In HVCD perovskite films, sharp and symmetric diffraction peaks of (100) and (200) planes were observed with no shoulder present.

Time-of-flight secondary-ion mass spectroscopy (ToF-SIMS) was further utilized to investigate the spatial vertical distribution of Cl^- anions. In the control film, pronounced Cl accumulations on both the top and bottom surfaces were observed (Fig. 1G), whereas throughout the HVCD films the distribution of Cl was uniform (Fig. 1H). These findings provided further evidence of the vertical inhomogeneity and surface accumulation of Cl in the control film, accounting for the distinct emission peaks from the top and buried surfaces in SSPL (Fig. 1A) and the shift of the diffraction peaks in GIXRD (Fig. 1E).

[1]State Key Laboratory of Semiconductor Physics and Chip Technologies, Institute of Semiconductors, Chinese Academy of Sciences, Beijing, P.R. China. [2]Center of Materials Science and Optoelectronics Engineering, University of Chinese Academy of Sciences, Beijing, P.R. China. [3]Laboratory of Advanced Optoelectronic Materials, Suzhou Key Laboratory of Novel Semiconductor-optoelectronics Materials and Devices, College of Chemistry, Chemical Engineering and Materials Science, Soochow University, Suzhou, China. ***Corresponding author. Email: jyou@semi.ac.cn (J.Y.)** †These authors contributed equally to this work.

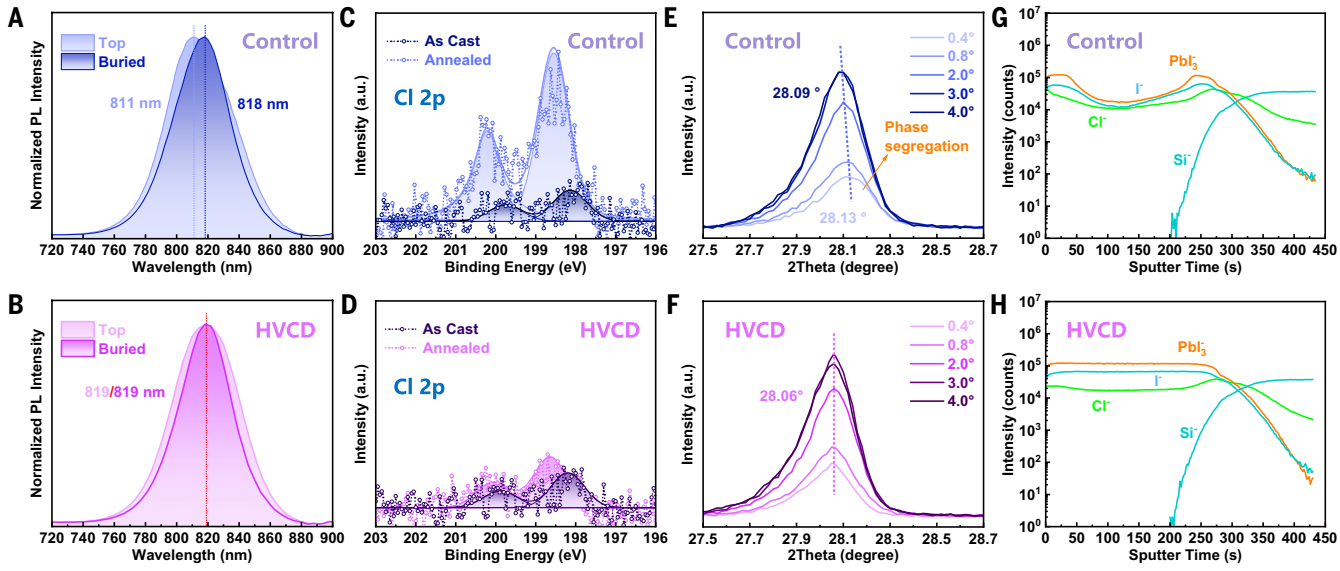

Fig. 1. Spatial vertical distribution of the perovskite phase and Cl anion. (**A** and **B**) SSPL from top and buried surface of control and HVCD films. (**C** and **D**) Cl 2p core energy spectra of control and HVCD films top surface before and after annealing. (**E** and **F**) GIXRD from the top surface of the control and HVCD perovskite films. (**G** and **H**) ToF-SIMS for the control and HVCD films.

Additionally, ToF-SIMS revealed the distribution of K^+ cations with a monotonic increasing intensity from the top surface to the substrate in the HVCD perovskite film (fig. S3). This behavior was likely attributed to the limited solubility of potassium salt in perovskite precursor, leading to their precipitation as supersaturation increased (table S1). The distribution trends of both Cl^- and K^+ in were further validated by the depth-profiling XPS results (fig. S4 and table S2). The weight ratio of K/Pb was 0.13 weight percent, which was quantified by inductively coupled plasma-mass spectrometry (fig. S5).

To elucidate the role of PB in the perovskite formation, XRD was employed to characterize the PbI_2-MACl systems both with and without PB incorporation. In the absence of PB, the XRD pattern of PbI_2-MACl exhibited a splitting of the (100) peak at 14.1° (fig. S6A), which we regarded as evidence of phase segregation resulting from the formation of Cl-incorporated $MAPbI_3$:Cl_x (*18*, *19*). Upon introduction of PB into PbI_2-MACl, the diffraction intensity associated with the Cl-incorporated $MAPbI_3$:Cl_x was substantially decreased, concomitant with the emergence of a new diffraction peak at 50.2° corresponding to the (222) plane of KCl (fig. S6B) (*20*). The formation of KCl suggested that PB facilitated the stabilization of Cl^-, thereby mitigating the rapid migration of Cl within the perovskite and suppressing the spatial vertical phase segregation (*21*). Theoretical calculations provided further evidence for the management of Cl during perovskite crystallization in the presence of PB (tables S3 to S6).

Surface morphology and properties

We used scanning electron microscopy (SEM) to image the surface morphologies of the control and HVCD perovskite films. The control perovskite film exhibited heterogeneous grain sizes and indistinct grain boundaries (Fig. 2A and fig. S7A), suggesting that the Cl accumulation inhibited coherent perovskite crystallization. The HVCD film demonstrated a uniform surface morphology with homogeneous and highly crystalline grains (Fig. 2B and fig. S7B). A narrow grain size distribution centered at 1.25 μm was obtained in the HVCD perovskite film, whereas the control films showed a broader distribution, with an average size of 0.9 μm (fig. S8). The improved crystalline quality of HVCD perovskite was consistent with the reduced full width at half maximum of the (100) diffraction peak in the XRD patterns (fig. S2). Atomic force microscope height images confirmed these observations (fig. S9). The enhanced crystallinity of perovskite was anticipated to prolong the charge carrier lifetimes and benefit charge transport.

After peeling the entire perovskite film off the fluorine-doped tin oxide (FTO)/nickel oxide (NiO_x) substrate with ultraviolet (UV)-activated glue, numerous cracks and pinholes were seen in the control film (Fig. 2C) whereas the HVCD film exhibited a continuous and smooth buried surface (Fig. 2D). The XPS results of the buried surfaces revealed an intensified Ni 2p in the HVCD films (fig. S10A), implying a more intimate and chemically robust NiO_x/perovskite interface. This enhanced interaction was likely attributed to the coordination between PB and NiO_x, which was also evidenced by the changes in the XRD patterns following PB incorporation (fig. S10B) (*22*, *23*).

To evaluate the surface homogeneity of the perovskite films, kelvin probe force microscopy (KPFM) was employed. The control film showed substantial fluctuations in surface potential (Fig. 2E), whereas a uniform distribution was observed in the HVCD film (Fig. 2F). The calculated work function of the HVCD film was 4.99 eV, slightly lower than that of the control film (5.08 eV). Photoluminescence (PL) mapping also suggested improved surface homogeneity of the HVCD perovskite films (fig. S11).

Based on all the results above, Fig. 2G show the proposed mechanism of the HVCD strategy on the regulation of Cl distribution (*24*–*26*). In the control perovskite film, the Cl^- anions separated from the $FAPbI_3$ lattice and migrated with the volatilization of solvents during annealing, resulting in Cl accumulation on the top surface. In the HVCD perovskite precursor, K^+ and $HC_2O_4^-$ dissociated to form an intermediate complex. During annealing, the separated free Cl^- anions rapidly formed a salt with K^+, which diffused in the opposite direction from the solvent and precipitated KCl near the buried interface. In addition, the pseudo halide binoxalate could modulate the crystal growth by forming an intermediate phase by means of chelating with unoccupied Pb (*27*–*29*), which could also be helpful in suppressing surface aggregation.

Optoelectronic properties of perovskite films

Because of the homogeneous Cl distribution, we anticipated that the HVCD film would have superior optoelectronic performance and more

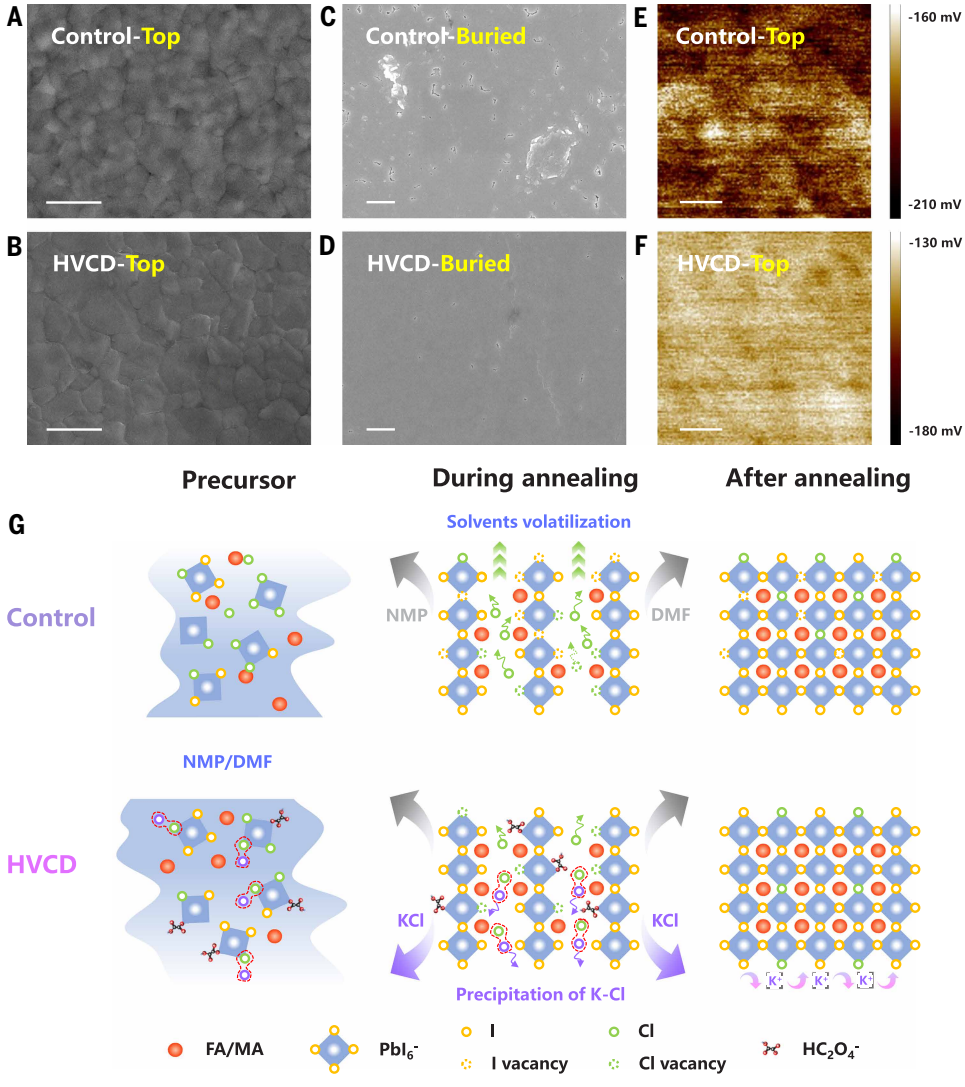

Fig. 2. Surface morphology and homogeneity of perovskite films, and film formation mechanisms. (**A** and **B**) Top-view SEM images of control and HVCD perovskite. (scale bar, 2 μm). (**C** and **D**) Buried-view SEM images of control and HVCD perovskite (scale bar, 2 μm). (**E** and **F**) Top surface KPFM image of control and HVCD films (scale bar, 1 μm). (**G**) Schematic diagram of the redistribution of Cl anions in the HVCD strategy. NMP, N-methyl-2-pyrrolidone; DMF, N,N-dimethylformamide; FA, formamidinium; MA, methylammonium.

efficient charge transfer characteristics compared with the control. We measured the photoluminescence quantum yield (PLQY) of the perovskite films from both the top and buried surfaces. The HVCD film showed a PLQY of 11.5 and 12.1% from top and buried surface, respectively, versus 5.9% (top surface) and 8.0% (buried surface) in the control film (Fig. 3A).

To further investigate the carrier recombination dynamics influenced by Cl distribution, time-resolved photoluminescence (TRPL) was performed on perovskite films deposited on a glass substrate. The carrier lifetimes measured from the top and bottom sides varied by a factor of 2 in control film, which were 1.2 μs and 2.3 μs, respectively, and both sides of the HVCD film consistently exhibited lifetimes of ~4 μs (Fig. 3B and table S7).

Also, we evaluated the charge transfer in the full device context: FTO/NiO_x/[4-(3,6-Dimethyl-9H-carbazol-9-yl) butyl] phosphonic acid (Me-4PACz)/control or HVCD perovskite/passivators/C_{60}. The electron extraction lifetime ($\tau 1$) at the perovskite/C_{60} interface decreased from 77.4 ns in the control to 49.3 ns in the HVCD film, indicating enhanced electron diffusion. Moreover, the HVCD perovskite film showed a substantially prolonged bulk lifetime ($\tau 2$) of 19.8 μs, versus 14.2 μs in the control (Fig. 3C and table S8) (*30*). Similar improvements were observed from the substrate side, which possibly resulted from the passivation of KCl at the buried interface (*31*–*33*). (fig. S12). Transient photovoltage (TPV) and transient photocurrent (TPC) measurements for the completed devices confirmed suppressed trap-assisted recombination and accelerated charge transfer kinetics in the HVCD devices, respectively (fig. S13).

We investigated the spatial distribution of charge carrier and trap densities throughout the perovskite layer by using drive-level capacitance profiling (DLCP) (*34*). Under high alternating current (ac) frequency bias, which primarily presented free carriers, the HVCD films showed increased free carrier densities at both the top and buried surfaces compared with the control (fig. S14). The total carrier density, measured under low ac frequency, was used to derive the trap density by subtracting the free carrier density. As shown in Fig. 3D, the HVCD film demonstrated a trap density of 1.65×10^{13} cm^{-3} at the top surface, which was one order of magnitude lower than the control (3.95×10^{14} cm^{-3}). Similarly, the trap density at the buried surface was reduced by a factor of three in the HVCD film compared to the control.

UV photoelectron spectroscopy (UPS) revealed that the work functions of control and HVCD perovskite films were 5.10 eV and 4.90 eV, respectively, and the valence band maximums (VBM) were estimated to be −6.06 eV and −5.74 eV, respectively (Fig. 3E). The optical bandgaps of the control and HVCD films, derived from Tauc plots based on UV-visible spectroscopy (UV-vis) (fig. S15), were consistent with SSPL results (Fig. 1, A and B). Energy level alignment at the perovskite/electron transport layer (ETL) interface was constructed based on the UPS results and the bandgap of the control (1.53 eV) and HVCD (1.51 eV) films from the PL and absorption results (Fig. 3F). The deeper-lying conduction band minimum (CBM) and the presence of an interfacial energy barrier in control film were expected to impede efficient electron extraction. The upshifted CBM and VBM in the HVCD film, which could be associated with the decreased Cl aggregation, eliminated the interfacial barrier and promoted better energy level alignment (*35*).

Device performance

We fabricated inverted perovskite solar cells with the architecture of FTO/NiO_x/Me-4PACz /$FAPbI_3$/passivators/C_{60}/SnO_2/Ag. The champion HVCD device achieved PCEs of 27.3 and 27.2% in reverse and forward scans, respectively, with negligible hysteresis, whereas the best control device yielded PCEs of 26.4 and 26.3% (reverse and forward scans, respectively) (Fig. 4A and table S9). The corresponding steady-state PCE of HVCD devices increased from 27.3 to 27.4% measured at maximum open circuit voltage (V_{OC}) for 5 min compared with the control (from 26.1 to 26.2%) (Fig. 4B). We also checked the device performance

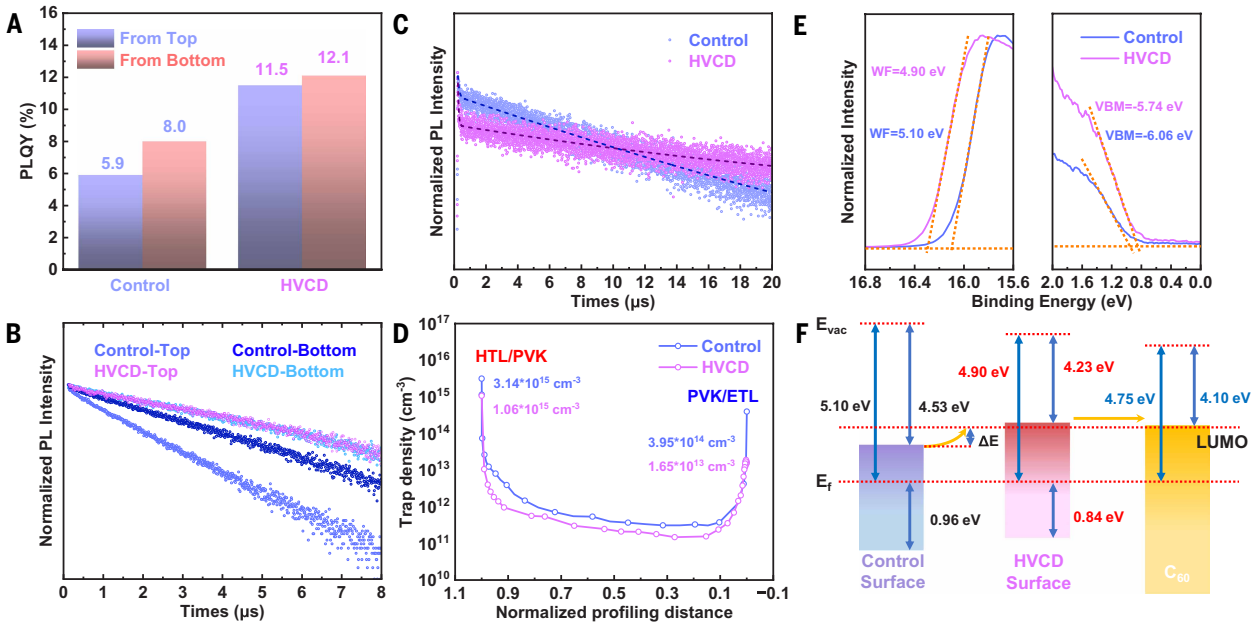

Fig. 3. Optoelectronic properties. (**A**) PLQY of control and HVCD films deposited on glass substrates without passivation measured from top and bottom. (**B**) TRPL spectra of control and HVCD films deposited on glass, which were measured from substrate and perovskite top surface, respectively. (**C**) TRPL spectra of FTO/HTL/perovskite/passivators/ETL, measured from ETL side. HTL, hole transport layer; ETL, electron transport layer. (**D**) Calculated trap density extracted from DLCP measurements for control and HVCD devices. PVK, perovskite. (**E**) UPS spectra of control and HVCD perovskite. (**F**) Band alignment at the interface between control or HVCD perovskite films and electron transport layer C_{60}.

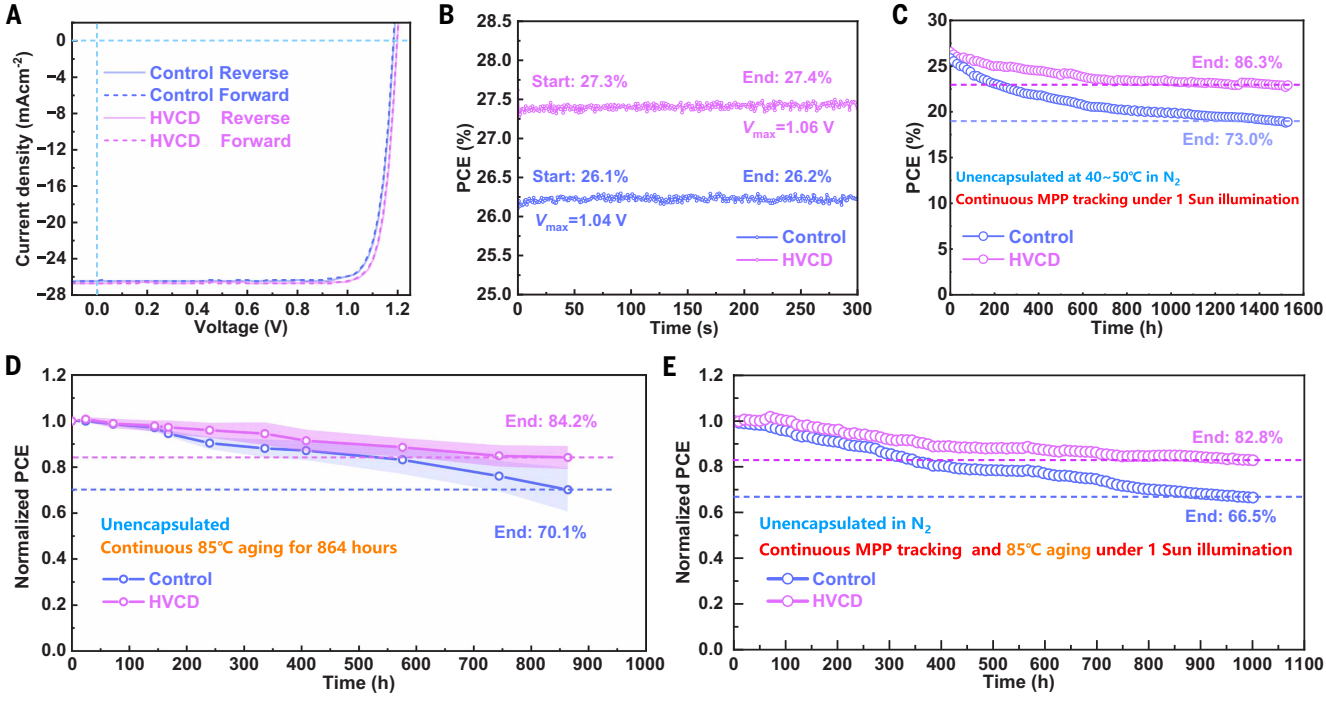

Fig. 4. Device performance and stability. (**A**) I-V characteristics of champion control and HVCD PSCs. The device area is 0.108 cm^2 and the measured mask size is 0.0725 cm^2. (**B**) Steady-state PCE of the control and HVCD devices measured under maximum power point for 5 min under AM1.5G 1 Sun illumination. (**C**) Continuous MPPT of control and HVCD devices under 1 Sun illumination (100 mW/cm^2) at 40~50°C. (**D**) Thermal stability of the control and HVCD perovskite solar cells aging at 85°C. (**E**) Continuous MPPT of control and HVCD devices under 1 Sun illumination and simultaneous 85°C aging.

while annealing the perovskite in ambient air with the relative humidity of 30 to 40%, which is a general procedure for MACl-containing perovskites (*36*, *37*). The performance of HVCD device was also better than that of the control (fig. S16A and table S10), although it was inferior to that of the devices processed in a nitrogen environment. We tested other alkali metal oxalates as an alternative additive, and a similar beneficial effect was validated using sodium oxalate (fig. S16B and table S11). The enhanced performance of HVCD devices primarily originated from the improvements in V_{OC} and the fill factor (*FF*), reaching values of 1.195 V and 85.6%, respectively, both approaching 95.6% of their theoretical limit (*38*, *39*). The short-circuit current densities (J_{SC}) of the control and HVCD devices were 26.4 mA cm^{-2} and 26.6 mA cm^{-2}, respectively, consistent with the external quantum efficiency (EQE) results (fig. S17). Additionally, the reproducibility of the HVCD strategy was confirmed across multiple device batches fabricated under varying external conditions (fig. S18).

We sent our champion devices to two accredited third-party institutions, the National Photovoltaic Industry Measurement Test Center (NPVM) and the National Institute of Metrology (NIM), for independent certifications. Both of the certified steady-state PCEs were 27.2% from NPVM (device area/measured mask area: 0.108 cm^2/0.074 cm^2) and NIM (device area/measured mask area: 0.135 cm^2/0.108 cm^2) (figs. S19 and S20). Also, PCEs of 26.4 and 26.2% from reverse and forward scans, respectively, have been achieved in the HVCD device with an active area of 1 cm^2 (fig. S21).

The presence of free Cl^- anion at interfaces and grain boundaries could introduce instability, which accelerated performance degradation over time under harsh conditions (*40*). We therefore measured the device stability under various conditions, including shelf stability, photo/thermal stability, or a combination thereof. Unencapsulated HVCD devices maintained 98.8% of their original PCE after >3000 hours in dark under an N_2 environment (fig. S22). The HVCD devices without reflection and encapsulation maintained 86.3% of their original PCE [26.6% measured at room temperature (RT)] after 1529 hours of MPPT under 1 Sun illumination (100 mW/cm^2) at 40~50°C in an N_2 environment, outperforming the control which retained only 73.0% (initial PCE of 25.9% measured at RT) (Fig. 4C and fig. S23).

To further confirm the improved stability after HVCD, we investigated the accelerated aging stability including thermal (85°C) and photothermal stability (MPPT at 85°C) of the devices. The HVCD device showed a T_{85} lifetime of 750 hours (initial PCE of 26.5% measured at RT) after 85°C aging, which was better than the control (initial PCE of 25.8% measured at RT) with 497 hours (Fig. 4D and fig. S24). By analyzing the behavior of the unpassivated devices upon 85°C aging (fig. S25), the performance decay in the passivated control device (Fig. 4D) was mainly caused by the degradation of both the perovskite and passivators, whereas the decline in the passivated HVCD device was mainly attributed to the passivators. As a result, we removed the passivation layer and then reevaluated the photothermal stability. The unpassivated HVCD device maintained 82.8% of its initial PCE (24.6%, measured at RT) after 1000 hours MPPT at 85°C, whereas the unpassivated control device degraded to 66.5% (initial PCE of 23.6% measured at RT) (Fig. 4E and fig. S26). From these results, it is unambiguous that the HVCD strategy enhanced both the device efficiency and stability by stabilizing the Cl with the formation of KCl and homogenizing the distribution of Cl^- anions that mitigated halide segregation.

Discussion

A PCE of >27% for perovskite solar cells with promising stability was obtained through the HVCD strategy. To further approach the theoretical limit of $FAPbI_3$ systems, we could focus on two aspects: (i) Although improved homogeneity of Cl distribution in the perovskite film was achieved by the HVCD strategy, further optimizations are required to achieve even more uniform phase distribution and reduced spatial heterogeneity. (ii) Although the defect density was reduced to 10^{13} cm^{-3} in the top surface, the buried interface still has a defect density as high as 10^{15} cm^{-3}, which requires a method to further reduce the buried interface defects.

REFERENCES AND NOTES

1. Y. Yang *et al.*, *Science* **386**, 898–902 (2024).
2. S. Liu *et al.*, *Nature* **632**, 536–542 (2024).
3. K. Zhao *et al.*, *Nature* **632**, 301–306 (2024).
4. P. Shi *et al.*, *Nature* **620**, 323–327 (2023).
5. M. Q. Tao *et al.*, *Joule* **8**, 3142–3152 (2024).
6. Y. Zhao *et al.*, *Science* **377**, 531–534 (2022).
7. J. Park *et al.*, *Nature* **616**, 724–730 (2023).
8. J. J. Zhou *et al.*, *Joule* **8**, 1691–1706 (2024).
9. L. Chen *et al.*, *J. Am. Chem. Soc.* **145**, 27900–27910 (2023).
10. J. You *et al.*, *Appl. Phys. Lett.* **105**, 183902 (2014).
11. K. Liu *et al.*, *Nat. Commun.* **13**, 4891 (2022).
12. Q. Jiang *et al.*, *Science* **378**, 1295–1300 (2022).
13. X. Y. Wu *et al.*, *Adv. Energy Mater.* **14**, 2304302 (2024).
14. S. Li *et al.*, *Nature* **635**, 82–88 (2024).
15. Z. Liang *et al.*, *Nature* **624**, 557–563 (2023).
16. Y. Bai *et al.*, *Science* **378**, 747–754 (2022).
17. C. Luo *et al.*, *Nat. Photonics* **17**, 856–864 (2023).
18. J. H. Noh, S. H. Im, J. H. Heo, T. N. Mandal, S. I. Seok, *Nano Lett.* **13**, 1764–1769 (2013).
19. J. Xu *et al.*, *Science* **367**, 1097–1104 (2020).
20. S. N. Ismail, E. M. Ali, B. J. Alwan, A. N. Abd, *Macromol. Symp.* **401**, 2100312 (2021).
21. F. Zheng *et al.*, *Adv. Energy Mater.* **9**, 1901016 (2019).
22. S. Yu *et al.*, *Science* **382**, 1399–1404 (2023).
23. J. Lee *et al.*, *Energy Environ. Sci.* **17**, 6003–6012 (2024).
24. X. Wang *et al.*, *Nat. Photonics* **18**, 1269–1275 (2024).
25. J. P. Perdew, K. Burke, M. Ernzerhof, *Phys. Rev. Lett.* **77**, 3865–3868 (1996).
26. S. Grimme, S. Ehrlich, L. Goerigk, *J. Comput. Chem.* **32**, 1456–1465 (2011).
27. L. Y. Yan *et al.*, *Nat. Energy* **8**, 1158–1167 (2023).
28. X. Xiao *et al.*, *Nature* **638**, 670–675 (2025).
29. J. Seo *et al.*, *Adv. Funct. Mater.* **35**, (2025).
30. J. Guo *et al.*, *Adv. Mater.* **35**, e2212126 (2023).
31. P. C. Zhu *et al.*, *Adv. Energy Mater.* **10**, 1903083 (2020).
32. L. P. Wang *et al.*, *Adv. Funct. Mater.* **32**, 2204725 (2022).
33. T. Bu *et al.*, *Nat. Commun.* **9**, 4609 (2018).
34. Y. Shen *et al.*, *Nature* **635**, 882–889 (2024).
35. S. Wang, T. Sakurai, W. Wen, Y. Qi, *Adv. Mater. Interfaces* **5**, 1800260 (2018).
36. Q. Jiang *et al.*, *Nat. Photonics* **13**, 460–466 (2019).
37. M. Kim *et al.*, *Joule* **3**, 2179–2192 (2019).
38. X. C. Li *et al.*, *Energy Environ. Sci.* **15**, 4813–4822 (2022).
39. J. Y. Huang *et al.*, *Adv. Energy Mater.* **14**, 2402469 (2024).
40. S. D. Stranks, H. J. Snaith, *Nat. Nanotechnol.* **10**, 391–402 (2015).

ACKNOWLEDGMENTS

We thank L. Meng from Institute of Chemistry, Chinese Academy of Sciences, and C. Guo from Tsinghua University for helping with the TPV measurements and Tof-SIMS measurement, respectively. **Funding:** This work was supported by the National Key Research and Development Program of China (grant 2024YFB4205200), the CAS Project for Young Scientists in Basic Research (grant YSBR-090), the National Natural Science Foundation of China (grant U24A6003), the Xiamen Fengyi Optoelectronic Technology Co., LTD and the Space Application System of China Manned Space Program (CMSS-2024-4-B-006). **Author contributions:** J.Y. and Z.X. conceived the idea; Z.X. fabricated and characterized the devices; Q.Z. participated in device fabrication and preparation for certification; S.K. and Y.L. carried out DLPC measurements; K.C., H.Z., Q.S., Z.H., Q.J., and X.Z. were involved in the data analysis; J.Y. directed and supervised the project; and J.Y. and Z.X. cowrote the manuscript. All authors contributed to discussions and finalizing the manuscript. **Competing interests:** A Chinese patent application (CN 202511213465. X) was submitted by the Institute of Semiconductors, CAS, which covers the homogenized vertical chlorine distribution (HVCD) strategy in perovskite films. **Data and materials availability:** All data needed to evaluate the conclusions in the paper are present in the paper or the supplementary materials.

SUPPLEMENTARY MATERIALS

science.org/doi/10.1126/science.adw8780
Materials and Methods; Supplementary Text; Figs. S1 to S26; Tables S1 to S11; References (*41*–*45*); Movie S1

Submitted 19 February 2025; resubmitted 30 May 2025; accepted 8 September 2025
10.1126/science.adw8780